Materials Science & Engineering A 974 (2026) 150844

Contents lists available at ScienceDirect

Materials Science & Engineering A

journal homepage: www.elsevier.com/locate/msea

Reduced low-temperature Charpy impact energy in additively manufactured duplex stainless steels

A.D. Iams [a,*], T.A. Palmer [b,c]

[a] Materials Science and Engineering Division, Materials Measurement Laboratory, National Institute of Standards and Technology, Gaithersburg, MD, 20899, USA
[b] Department of Engineering Science and Mechanics, Pennsylvania State University, University Park, PA, 16802, USA
[c] Department of Materials Science and Engineering, Pennsylvania State University, University Park, PA, 16802, USA

ARTICLE INFO

Keywords:
Additive manufacturing
Directed energy deposition
Hot isostatic pressing
Duplex stainless steel
Oxide inclusions
Charpy impact testing

ABSTRACT

Room temperature tensile properties for standard and super duplex stainless steels fabricated using directed energy deposition additive manufacturing meet and even exceed those observed in the wrought condition. However, the performance of these alloys in the as-deposited condition under Charpy impact testing at −46 °C was significantly degraded, falling far below that observed in wrought products. The reduced impact energy resulted from a combination of process-related defects, unfavorable ferrite-austenite phase fraction and size, and a network of oxygen-rich inclusions. Crack propagation occurred relatively unobstructed through the brittle ferritic matrix and fine intragranular austenite, indicating limited resistance to fracture in these regions. Post-process hot isostatic pressing eliminated process-related defects and increased both the austenite phase fraction and size, resulting in improved impact energy. A more tortuous crack path was observed, with cracks both cutting through and propagating parallel to coarser austenite features, suggesting enhanced crack deflection and increased resistance to propagation. Despite these improvements, impact energies remained significantly below those observed in the corresponding wrought materials due to the formation of thermodynamically stable oxygen-rich inclusions, which originated in the powder feedstock that displayed oxygen contents 5 to 20 times higher than those observed in the wrought materials.

1. Introduction

Wrought duplex stainless steels (DSS) undergo a series of controlled thermomechanical treatments to obtain a balanced microstructure comprised of nearly equal phase fractions of ferrite and austenite. This dual phase microstructure contributes to their high strength and impact energy, and superior corrosion resistance, making these alloys attractive for use in the oil and natural gas industries [1]. However, DSS alloys are available in a limited number of product forms, requiring the implementation of various forming, welding and joining processes to produce components with complex geometries [2]. The thermal histories inherent to these processing routes can disrupt the ferrite-austenite phase balance and lead to the formation of undesirable secondary phases, such as sigma phase [3], that degrade their mechanical and corrosion properties [4,5].

Additive manufacturing (AM) processes provide the promise of producing more complex product forms and providing increased design flexibility independent of the post-processing required in traditional wrought manufacturing operations [6]. Powder bed fusion (PBF) [7–19] and directed energy deposition (DED) [20–27] AM techniques are being explored as alternative processing routes for both existing and new DSS components. These AM processes are characterized by rapid heating, melting, solidification, and cooling cycles that produce microstructures that are far different from those observed in their wrought DSS counterparts. Differences in the AM processing route and selection of the heat source can also alter the cooling rates during solidification, leading to differences in both microstructures and mechanical properties, which are summarized in Table A1.

For instance, laser-based powder bed fusion (PBF-L) processes are frequently used to process wrought DSS grades and are characterized by solidification cooling rates on the order of 10^5 K/s to 10^6 K/s [6]. With such rapid cooling rates, almost entirely ferritic microstructures (~99 %) are produced in the as-deposited condition, resulting in high yield and ultimate strength values, and low elongations [7–16]. As shown in Fig. 1, PBF-L processed DSS alloys tested in the as-deposited condition displayed mean yield and ultimate strengths on the order of 890 MPa and 1035 MPa, respectively. While these strength levels generally met the standard requirement for wrought materials [26], the AM materials tended to display elongations below the specified minimums [26]. Post-process heat treatments (HT), even at relatively short durations, restore the elongation values in both grades to levels consistent with standard wrought requirements as more balanced

* Corresponding author.
E-mail address: andrew.iams@nist.gov (A.D. Iams).

https://doi.org/10.1016/j.msea.2026.150844
Received 17 April 2026; Received in revised form 10 July 2026; Accepted 26 July 2026
Available online 27 July 2026
0921-5093/Published by Elsevier B.V.

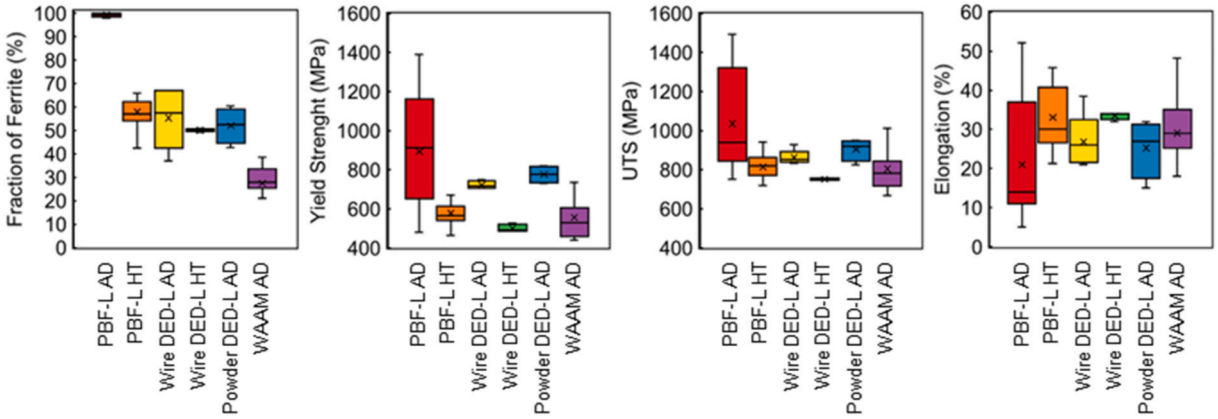

Fig. 1. Comparison of ferrite fraction and tensile properties of additively manufactured duplex stainless steels by processing route. Data are summarized from Table A1. When ranges were reported in the literature, the median of the reported range was used for analysis. X-axis labels follow the format process–condition (e.g., PBF-L AD), where AD: as-deposited and HT: heat treated. Some data were obtained using miniature tensile specimens, which can provide comparable yield and ultimate tensile strength values to standard specimens [28]. However, elongation is sensitive to specimen geometry [28] and should therefore be interpreted with caution.

ferrite-austenite levels were achieved.

DED processes tend to be more flexible than PBF processes, particularly in the selection of the energy source (laser or arc) and the feedstock form (powder or wire). The use of arc-based energy sources in conjunction with wire feedstocks, typically referred to as wire arc additive manufacturing (WAAM), has been the most popular technique for fabricating DSS components [27,29–38], as displayed in Table A1. Decreased cooling rates, on the order of 10^2 K/s to 10^4 K/s during solidification [6], produce as-deposited microstructures with austenite fractions (~70 %) far higher than their PBF-L counterparts [7–16], as highlighted in Fig. 1. These increased austenite levels result from the slower cooling rates experienced with the arc heat source and the higher nickel contents in the wire feedstocks, which have been traditionally used to promote balanced microstructures in arc welding applications [5]. With the high levels of austenite in the WAAM microstructures, strength and elongation measurements tend to meet the minimum standard wrought values in the absence of additional post-process heat treatment.

Of the DED processes, several studies have investigated laser-based directed energy deposition (DED-L) coupled with powder feedstocks [20–26]. This processing pathway enables the use of traditional wrought compositions for both standard and super DSS grade components [20–26]. Solidification cooling rates in DED-L typically fall between those that are characteristic of PBF-L and WAAM [6]. Under these conditions, more balanced microstructures are commonly obtained without the need for high-nickel filler metals, as summarized in Fig. 1. With this balanced microstructure, tensile properties tend to fall between those reported for PBF-L and WAAM in both the as-deposited and post-processed conditions.

Although the AM DSS literature frequently emphasizes favorable room-temperature tensile properties, and these properties often appear to exceed wrought requirements, they do not support operation for harsh service environments. Certification for more aggressive applications requires testing under more representative conditions, including low-temperature impact testing. For example, welded standard and super DSS alloys used in the oil and gas industries must display a minimum average impact energy of 45 J at a temperature of −46 °C [39].

As shown in Table A2, there is limited low-temperature full-size Charpy impact testing data available for PBF-L processed DSS alloys, but the available results obtained during room temperature testing indicate a strong dependence of impact performance on processing route and the resulting ferrite/austenite phase balance [12]. For instance, as-deposited materials with a primarily ferritic microstructure displayed an average room temperature impact energy of 18 J ± 3 J [12]. Following post-process heat treatment, the austenite fraction increased to nearly 40 %, and the impact energy increased to 132 J ± 5 J, highlighting the critical role of phase balance on the impact energy [12]. In contrast, full-size impact test specimens for DSS alloys fabricated by WAAM [30,31,37,40] and DED-L [21,22], displayed higher austenite fractions driven by lower effective cooling rates and nickel-enriched wire feedstocks. The impact energies of these materials were similar to wrought, even in the as-deposited condition.

In addition to the processing route and ferrite/austenite phase fractions, another important factor that influences impact energy is oxygen content. The impact energy of DSS alloys can be sensitive to oxygen, which promotes the formation of oxide inclusions [25] that degrade impact performance [41]. Although the available experimental data are limited [41,42], the results summarized in Fig. 2 indicate that increased oxygen content in materials produced by welding and powder metallurgy routes is generally associated with reduced impact energy. However, oxygen is rarely reported in the AM DSS literature, likely because it is low in wrought products and is not generally included as part of standard compositional specifications [43]. For example, of the 28 impact energy data points within Table A2, bulk oxygen content was reported for only 15 data points.

Taken together, the limited availability of low-temperature Charpy data and the inconsistent reporting of oxygen content make it difficult to assess whether AM DSS alloys can meet impact testing requirements for demanding service environments. To address this gap, Charpy impact testing was conducted on both standard (UNS S32205) and super (UNS S32750) DSS alloys fabricated using a DED-L AM process with powder feedstocks. While the room temperature tensile properties met or exceeded those of wrought materials, testing these AM materials under low-temperature impact loading conditions revealed a notable degradation in properties and performance. At these low temperatures, complex interactions among process-related defects, the ferrite and austenite phases, and a network of oxygen-rich inclusions led to extremely low impact energies and primarily brittle failure modes. With the addition of a post-process hot isostatic pressing (HIP) treatment, these low-temperature impact properties were enhanced as the austenite phases increased in size and became more interconnected, but remained significantly below those observed in the corresponding wrought alloys.

2. Experimental

A series of standard (UNS S32205) and super (UNS S32750) DSS (Sandvik Osprey, Neath, UK[1]) wall structures that were approximately

[1] Certain commercial equipment, instruments, software, or materials are identified in this paper to foster understanding. Such identification does not imply recommendation or endorsement by the Department of Commerce or the National Institute of Standards and Technology, nor does it imply that the materials or equipment identified are necessarily the best available for the purpose.

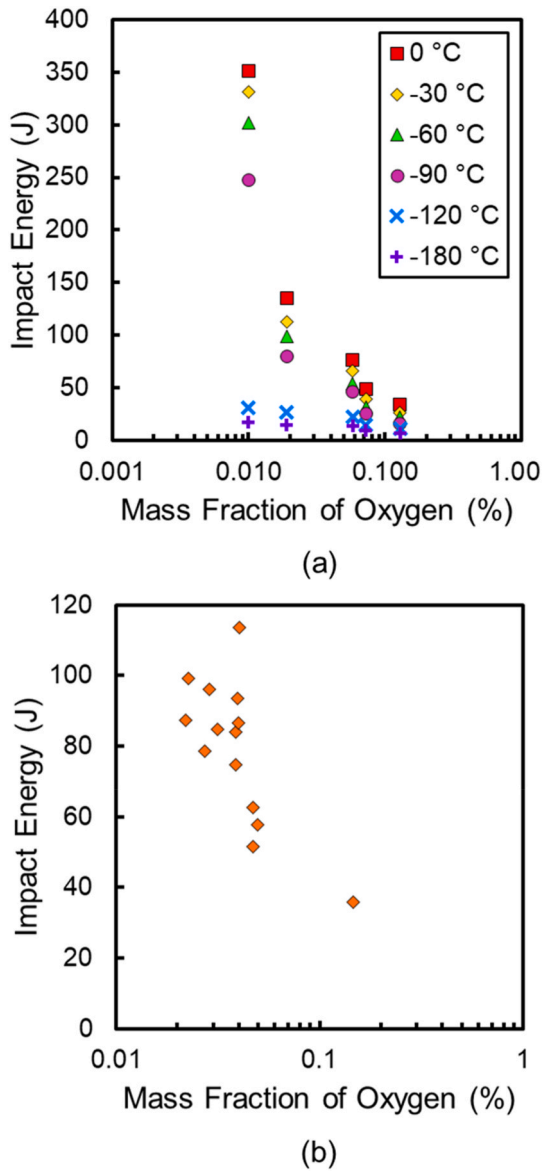

Fig. 2. Impact energy as a function of oxygen content for duplex stainless steel alloys fabricated by (a) welding [41] and (b) powder metallurgy (PM) [42] processes. For the welding data, impact testing was conducted at various temperatures using 2209 filler material. For the PM data, impact testing was conducted at −20 °C using a high-alloy PM + HIP duplex stainless steel.

102 mm long by 102 mm tall and 13 mm wide were fabricated using a DED-L AM process with powder feedstock in an environmentally controlled argon atmosphere. During deposition, a YLR-12000 ytterbium fiber laser (IPG Photonics[1], Oxford, US) with a wavelength between 1070 nm and 1080 nm, was operated at a laser power of 2000 W and a beam diameter of approximately 4 mm. Powder was coaxially fed to the melt pool through four nozzles at a total mass flow rate of 15 g/min, and each deposition pass was made at a travel speed of 10.6 mm/s with a hatch spacing of 2.5 mm between individual passes. These deposition parameters produced individual layers with a height of approximately 0.9 mm. Details of the deposition system and the processing of these structures are provided elsewhere [24,25].

The DSS alloy powders used to fabricate these structures had a particle size range between 53 µm and 150 µm. Compositions of the as-deposited materials were measured using standard techniques [44,45] at a certified testing laboratory (Luvak Laboratories[1], Boylston, US) and are listed in Table 1 and generally fell within the specified composition ranges [43]. Additional measurements of the oxygen composition were also performed using an inert gas fusion technique [44]. Selected wall structures in the as-deposited material condition were subjected to post-process HIP (Quintus Technologies[1] AMD Application Center, Columbus, US) at a temperature of 1170 °C and pressure of 145 MPa for 3 h. At the completion of the cycle, the material was cooled to a temperature of 200 °C at a rate of 2.1 °C/s inside the HIP chamber, then removed and allowed to air cool to room temperature.

In order to measure the size and location of process defects in each wall structure, a Phoenix v|tome|x m X-ray computed tomography (CT) system (GE Sensing & Inspection Technologies[1], Cincinnati, US) was operated at an accelerating voltage of 250 kV and a beam current of 150 µA. Individual images were compiled to form 3D images using ImageJ Fiji, which is an open-source image-processing platform (National Institutes of Health, Bethesda, US). Additional data visualization and analysis were then performed on the images using Avizo 9.7.0 (Thermo Fisher Scientific[1], Waltham, US).

After fabrication and post-processing, tensile and Charpy impact testing specimens were extracted from specific locations at orientations parallel (longitudinal) and perpendicular (transverse) to the deposition direction, as shown in Fig. 3. All tensile testing specimens were scaled to 40 % of the standard subsize rectangular tensile specimen [46] dimensions with a gauge length of 10 mm, a width and thickness of 2.4 mm, and a reduced section length of 14.4 mm. Uniaxial tensile testing was conducted on an MTS Criterion Model 43 (MTS[1], Eden Prairie, US) electromechanical test system using a 20 kN load cell coupled with a video extensometer. Tests were conducted at room temperature using cross-head speed control, at a speed of 0.22 mm/min. The 0.2 % offset yield strength, tensile strength, and the elongation at fracture were obtained from the resulting engineering stress-strain curves. Full-size standard v-notch Charpy impact test specimens [47]

Table 1
Chemical composition of the standard and super grades of duplex stainless steel. Data presented as mass fraction (%).

		Standard (UNS S32205)			Super (UNS S32750)		
Element	Measurement Uncertainty	ASTM [43]	Wrought	AD	ASTM [43]	Wrought	AD
Cr	±0.5	22.0 – 23.0	22.8	22.2	24.0 – 26.0	25.0	24.5
Ni	±0.2	4.5 – 6.5	5.5	5.8	6.0 – 8.0	7.1	7.3
Mo	±0.06	3.0 – 3.5	3.2	3.2	3.0 – 5.0	3.9	4.0
Mn	±0.05	2.00	1.9	1.3	1.20	0.77	0.91
Si	±0.05	1.00	0.55	0.83	0.80	0.37	0.52
N	±0.02	0.14 – 0.20	0.16	0.19	0.24 – 0.32	0.34	0.29
C	±0.005	0.03	0.014	0.020	0.030	0.024	0.020
P	±0.002	0.03	0.017	0.004	0.035	0.028	0.017
S	±0.002	0.02	0.0005	0.006	0.020	0.0005	0.008
O	±0.005	N/A	0.006	0.033	N/A	0.0043	0.094
Fe	---	Bal.	Bal.	Bal.	Bal.	Bal.	Bal.

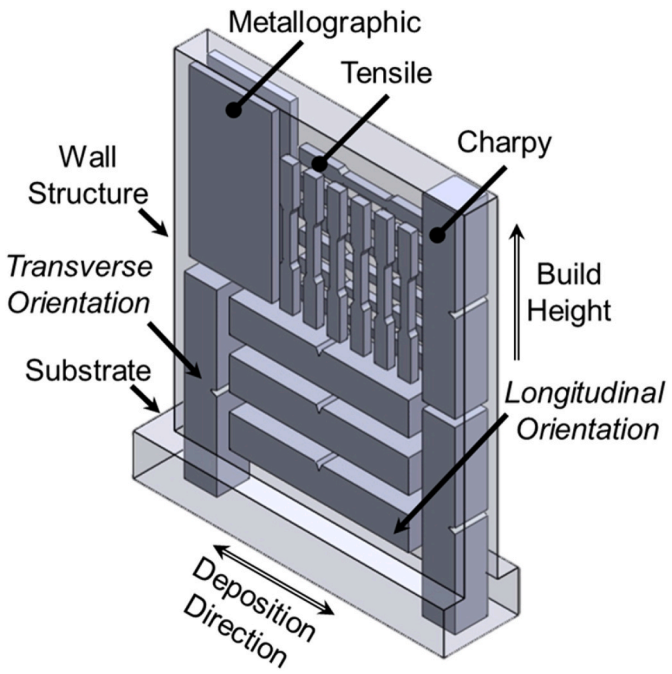

Fig. 3. Schematic showing the locations of metallographic, tensile, and Charpy impact specimens within the additively manufactured wall structure.

with a length of 55 mm, and a cross-sectional area of 100 mm^2 (10 mm x 10 mm) were then tested at −46 °C at a certified laboratory (WTTI[1], Allentown, US). Equivalent wrought standard grade and super grade duplex stainless steel alloys were evaluated and tested in the same manner.

Metallographic specimens were also extracted from the wall structures for each material and processing condition, as shown schematically in Fig. 3. After mounting in a thermo-setting epoxy, these specimens were ground using SiC grinding paper to P4000 ISO grit size and polished using a 3 μm diamond slurry followed by a 1 μm diamond slurry. Final polishing was then performed using a 0.06 μm colloidal silica solution. Samples prepared for characterization using optical microscopy were etched using a KOH electrolytic solution (25 g KOH, 50 mL distilled water, 5 V DC for 5 s) to reveal the austenite and ferrite phases and to distinguish between the different austenite morphologies. Images were obtained using an Epiphot (Nikon Corporation[1], Tokyo, JP) inverted microscope with a DS-Fi3 camera (Nikon Corporation[1], Tokyo, JP). Images of fracture surfaces and unetched samples were obtained using an Apreo S Scanning Electron Microscope (SEM) (Thermo Fisher Scientific[1], Waltham, US), with an EDS X-MaxN detector (Oxford Instruments[1], Abingdon, UK). Electron backscatter diffraction (EBSD) images of unetched samples were collected using a JEOL 7100 SEM system (JEOL Ltd.[1], Tokyo, JP) equipped with a Symmetry S2 detector (Oxford Instruments[1], Abingdon, UK). EBSD measurements were taken at an operating voltage of 20 kV and a current of 5.0 nA, with a step size of 0.25 μm. Energy-dispersive X-ray spectroscopy (EDS) and EBSD data were collected and analyzed using the AZtec software suite (Oxford Instruments[1], Abingdon, UK).

Number densities and sizes of the inclusions present in the as-deposited and post-processed HIP materials were measured at multiple locations in each specimen across an area of approximately 46,638 μm^2 using the ImageJ[1] software package (National Institutes of Health, Bethesda, US). Manual thresholding was used to segment the inclusions. Fixed lower and upper grayscale intensity values were determined and

Table 2
Summary of room temperature tensile and low-temperature Charpy impact properties.

Grade	Condition	Orientation[a]	Yield Strength[b c] (MPa)	UTS[b c] (MPa)	Elongation[b c] (%)	Impact Energy[b] (J)
Standard	As-Deposited	**Avg**[d]	**613 ± 11**	**847 ± 41**	**25 ± 15**	**13 ± 5**
		L	608 ± 9	871 ± 12	38 ± 3	16 ± 4
		T	618 ± 10	823 ± 46	11 ± 7[e]	10 ± 4
	Post-Process HIP	**Avg**[d]	**493 ± 15**	**767 ± 18**	**43 ± 12**	**50 ± 27**
		L	495 ± 20	770 ± 15	49 ± 1	71 ± 17
		T	491 ± 8	764 ± 17	42 ± 5	28 ± 12
	Wrought	**Avg**[d]	**560 ± 36**	**733 ± 27**	**47 ± 5**	**152 ± 32**
		RD	584 ± 22	753 ± 9	44 ± 5	171 ± 21
		TR	535 ± 32	714 ± 23	50 ± 4	122 ± 19
	Standard Requirement	N/A	450[f]	655[f]	25[f]	45[g]
Super	As-Deposited	**Avg**[d]	**648 ± 26**	**885 ± 47**	**24 ± 12**	**16 ± 9**
		L	650 ± 32	911 ± 26	35 ± 3	24 ± 7
		T	645 ± 18	858 ± 47	13 ± 5[d]	9 ± 1
	Post-Process HIP	**Avg**[d]	**519 ± 40**	**847 ± 39**	**44 ± 3**	**27 ± 11**
		L	520 ± 25	847 ± 34	41 ± 3	35 ± 4
		T	517 ± 51	847 ± 44	46 ± 2	18 ± 7
	Wrought	**Avg**[d]	**625 ± 38**	**855 ± 14**	**54 ± 3**	**144 ± 36**
		RD	645 ± 46	854 ± 22	55 ± 4	177 ± 7
		TR	604 ± 15	855 ± 5	54 ± 1	112 ± 12
	Standard Requirement	N/A	515[f]	760[f]	15[f]	45[g]

Notes:
[a] Orientation is defined according to schematic shown in Fig. 3, where, L = longitudinal, T = transverse, RD = rolling direction, TR = transverse rolling direction (perpendicular to rolling direction).
[b] Tensile samples were tested at room temperature (RT) at 23 °C, while Charpy impact samples were tested at −46 °C.
[c] Tensile data were obtained using miniature specimens, which can provide comparable yield and ultimate tensile strength values to standard specimens [47]. However, elongation is sensitive to specimen geometry [28] and should therefore be interpreted with caution.
[d] The data are averages of all the longitudinal and transverse orientation data.
[e] The low elongation values were a result of process-related defects within the gauge section of the tensile samples, as shown in Fig. 5.
[f] Minimum requirement according to ASTM A276 [43].
[g] Minimum requirement for quality level II forgings, castings, and HIP products according to ISO 17781 [39].

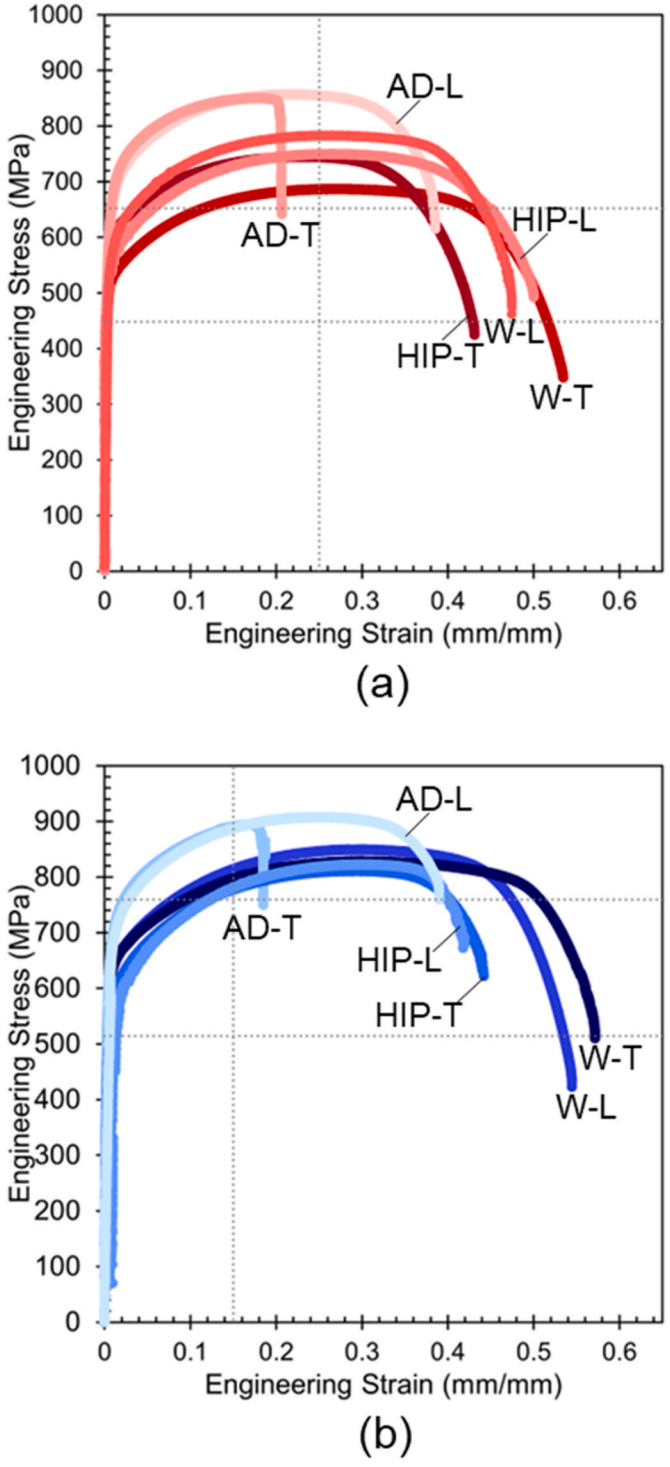

Fig. 4. Engineering stress-strain curves tested at room temperature for the (a) standard and (b) super grades of duplex stainless steel. The standard requirements [39,43] are represented by the dotted lines.

applied uniformly across all images to ensure consistency and reproducibility. To accommodate non-uniform shapes for the particles, the measured area of each particle was converted to a circular equivalent (CE) diameter value. Inclusions with a CE diameter of less than 100 nm fell below the resolution limits of the captured images and were removed from the statistical analysis.

3. Results and discussion

3.1. Room temperature tensile properties

Room-temperature tensile properties of DED-L standard and super DSS grades met the minimum standard wrought material requirements and displayed average yield and ultimate tensile strengths exceeding those measured for companion wrought materials, as summarized in Table 2. Even though these average values are generally acceptable, there are several outliers. For example, examination of the individual engineering stress-strain curves showed that the elongation to failure of several as-deposited specimens fell below specified minimum values, highlighted in Fig. 4. However, when averaged, the nominal elongation values met the minimum requirements of 25 % and 15 % for the standard and super DSS grades, respectively [43]. These average values had large standard deviations and, in some cases, were close to the standard limit. Therefore, these elongation results should be interpreted with caution because they were obtained using miniature tensile specimens, for which elongation is sensitive to specimen geometry [28]. In contrast, miniature tensile specimens have been shown to provide yield and ultimate tensile strength values comparable to those obtained from standard specimens [28].

In the as-deposited condition, the elongation values of the DSS grades exhibit a strong dependence on build orientation. The most pronounced loss of ductility occurs in specimens tested in the transverse orientation, where the standard and super grades displayed elongation values of 11 % ± 7 % and 13 % ± 5 %, respectively. The transverse orientation data did not meet the minimum standard requirement and displayed significant scatter, which was the main contributor to the large standard deviations in Table 2. In contrast, samples tested in the longitudinal orientation met the minimum standard requirements with significantly less scatter. Despite this improvement, the nominal elongation values, on the order of 30 % for both DSS grades, remain below those of wrought materials, which are often near 50 %.

Decreases in elongation to failure in similarly processed AM materials have been previously attributed to the presence of process-related defects [48] resulting from gas porosity or lack-of-fusion defects [49]. These process-related defects are typically quantified by a measurement of the volume fraction of porosity present in the builds, which was performed here and is summarized in Table 3. While the gross measurements of the builds showed low porosity fractions, localized defects were observed within the gauge section of tensile samples, as shown in Fig. 5. For example, while gross porosity measurements for the standard grade were approximately 0.02 %, the transverse orientated tensile specimens contained localized defects within the gauge section that occupied between 2 % and 3 % of the cross-sectional area. Therefore, the 2 % to 3 % value should be interpreted as a measurement through a defect-rich region of the tensile specimen, rather than a reflection of the average porosity of the build.

The location and morphology of these defects along with the build direction and resulting deposition layers contributed to this decrease in the elongation to failure in the as-deposited DSS materials. Clear differences in the fracture surface appearance and crack propagation behavior were observed between specimens tested in the longitudinal and transverse orientations. As shown in Fig. 6(a) and (b), the longitudinal specimen exhibits a tortuous fracture path, whereas the transverse specimen shows a comparatively flat surface aligned parallel to the deposition layers. During the testing of the transverse specimens, the loading direction was perpendicular to the build layers and the lack-of-fusion defects. A closer examination of the transverse fracture surface in Fig. 6(b) revealed partially melted powder particles in the regions where these defects were detected. The presence of these partially melted powder particles indicated the defect type was a lack-of-fusion defect [49], and further highlighting the role that the process-related defects played in driving crack propagation and how they contributed to the reduced elongation at failure values in the as-deposited materials.

Table 3
Microstructural and porosity data for standard and super duplex stainless steel.

Grade	Condition	Porosity Fraction[a] (%)	Austenite Fraction (%)	Average Austenite Grain Size[c] (μm)	Average Ferrite Grain Size[c] (μm)	Average Inclusion Size[c] (nm)	Inclusion Number Density (inclusions /mm^2)
Standard	As-Deposited	0.018	51 ± 1	5 ± 3	19 ± 6	223 ± 73	2.76×10^4
	Post-Process HIP	---[b]	57 ± 3	10 ± 6	21 ± 12	245 ± 154	2.46×10^4
Super	As-Deposited	0.011	61 ± 1	6 ± 5	15 ± 6	314 ± 142	3.48×10^4
	Post-Process HIP	---[b]	63 ± 3	11 ± 6	14 ± 5	272 ± 152	3.07×10^4

Notes:
[a] The porosity fraction was determined from X-ray CT measurements.
[b] No porosity was detected using the X-ray CT parameters identified within the experimental procedures.
[c] Grain and inclusion sizes are presented as circular equivalent diameter.

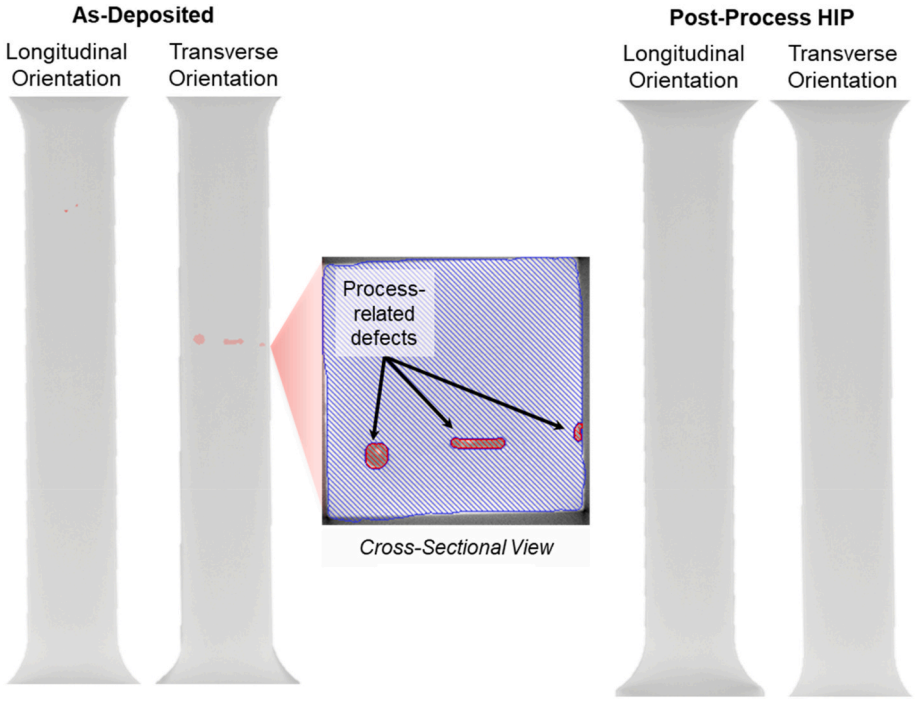

Fig. 5. Reconstructed X-ray CT images of the gauge section tensile samples in both the as-deposited and post-processed HIP condition, showing process-related defects within the as-deposited transversely oriented sample.

The application of a HIP post-processing step provided a means for removing these process-related defects, as highlighted in Table 3 and Fig. 5. At the same time, a more uniform microstructure was produced. As shown in Fig. 6(c) and (d), the prominent deposition layers observed in the as-deposited material were eliminated and the austenite morphology became more similar in appearance to that present in cast and wrought materials. Along with these changes in microstructure, the post-processed AM standard and super DSS grades also exhibited different room temperature tensile properties. As shown in Table 2, the yield strength in the HIP post-processed materials was reduced by approximately 20 % for both grades. Despite this decrease, the nominal yield strength remained above the minimum standard requirements but was lower than those measured in the wrought materials. Ultimate tensile strength (UTS) values were also reduced by 10 % in the standard grade and 5 % in the super grade, but still met the minimum requirements [43] and were equivalent to the wrought counterparts. In contrast to these reductions in strength, elongation to failure improved, increasing by nearly 70 % compared to the as-deposited condition. The observed reductions in strength and concurrent increases in elongation are consistent with expected trends for other AM alloys following HIP [14], reflecting the combined effects of pore elimination and a homogenous microstructure on tensile performance.

Even though the room temperature tensile property data for the as-deposited and post-process HIP materials differ, they generally exceed minimum standard wrought values [43], making them attractive alternatives to traditional wrought products. However, small deviations from nominal wrought properties remain, particularly in the elongation of the super grade, indicating that differences persist even with the addition of a HIP post-processing step. Overall, this combination of defect elimination and a uniform microstructure obtained with this post-processing step led to higher elongation values with reduced scatter, that met the minimum standard requirements [43] and were similar to wrought values.

3.2. Fractographic analysis of tensile specimens

The mechanisms underlying this mechanical response can be examined through the features observed on the representative fracture

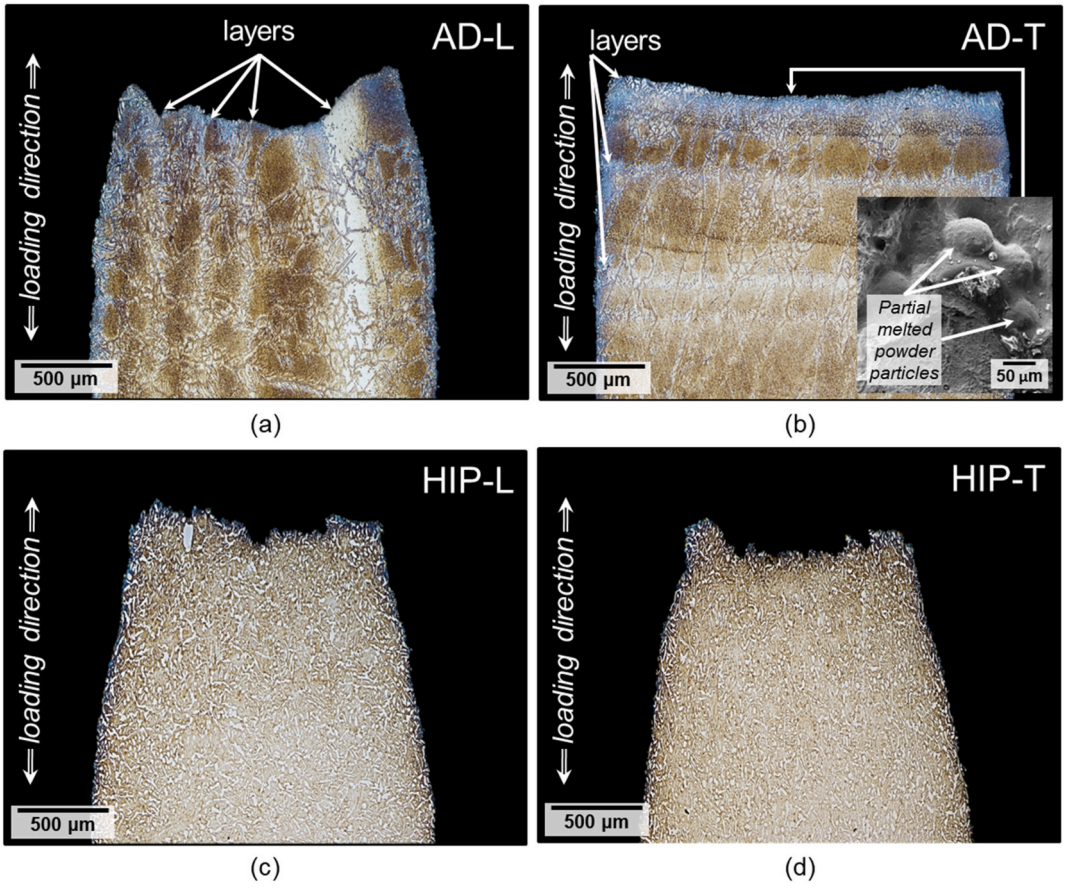

Fig. 6. A representative profile view of broken tensile samples in the (a)(c) longitudinal and (b)(d) transverse orientations of a standard grade of duplex stainless steel in the (a)(b) as-deposited and (c)(d) post-process HIP conditions.

surfaces. Fig. 7 highlights the different fracture surface features for the as-deposited and the post-process HIP conditions, respectively. Each fracture surface displayed equiaxed dimpled morphologies, indicating a ductile fracture mode. More importantly, however, was the appearance of extensive networks of inclusions within the dimples on the fracture surfaces. These inclusions appear to act as nucleation sites for microvoid formation during deformation, suggesting that they play a role in controlling the fracture behavior of the AM materials.

The origin of these inclusions can be traced to oxygen present within the powder feedstocks used during the AM process. Although they are frequently not included in compositional specifications or even measured, interstitial alloying elements, such as nitrogen and oxygen, can influence microstructural evolution and secondary phase formation [25,50–54]. For example, in standard (UNS S32205) and super (UNS S32750) DSS grades, the as-deposited microstructure was dominated by fine intragranular austenite that nucleated on oxide inclusions [24] originating from the powder feedstocks, which contained oxygen on the order of 0.01 % to 0.1 % mass fraction. These inclusions persisted through deposition and post-process HIP, evolving from a primarily amorphous structure to different crystalline structures, depending on the alloy composition [25].

Compositional mapping of these inclusions provides insight into the oxides present within the microstructures. In the as-deposited condition for both DSS grades, the inclusions are rich in Cr, Mn, Si, and O, which is consistent with the combination of spinel ($MnCr_2O_4$) and rhodonite ($MnSiO_3$) inclusions observed in these alloys [25]. With HIP post-processing, the inclusions are primarily composed of Cr, Mn, and O, indicating that the inclusions are transforming from the combination of metastable rhodonite and spinel to primarily stable spinel inclusions [25]. As the matrix microstructure evolves during the HIP post-processing step, these oxide inclusions persist due to their high thermodynamic stability [25]. In contrast, wrought materials typically contain significantly lower oxygen levels, resulting in fewer oxide inclusions [25]. The persistence of these oxide inclusions in AM materials, despite reductions in defects and microstructure homogenization during HIP, likely contributes to the reduction in elongation relative to wrought materials.

3.3. Low-temperature Charpy impact properties

While the measurement of room temperature tensile properties is a common metric for evaluating AM materials, it provides little insight into their performance under service-relevant conditions. Additional testing is often required for specific applications to ensure reliability under more demanding conditions. For example, low-temperature impact testing at a temperature of −46 °C is required for DSS alloys used in the oil and gas industry [39]. Even under these rather extreme conditions, cast and wrought DSS alloys commonly display high levels of impact energy, exceeding the minimum requirement of 45 J [1]. Since equivalent AM processed DSS grades are expected to replace cast or wrought materials operating under these same service conditions, the ability of AM materials to exhibit similar performance and properties, and meet minimum requirements, will be expected.

A significant decrease in the measured low-temperature impact energies compared with wrought materials was observed when Charpy impact testing was performed on as-deposited standard and super DSS grades. The measured impact energies for the wrought materials were approximately 9 to 12 times greater than their corresponding AM

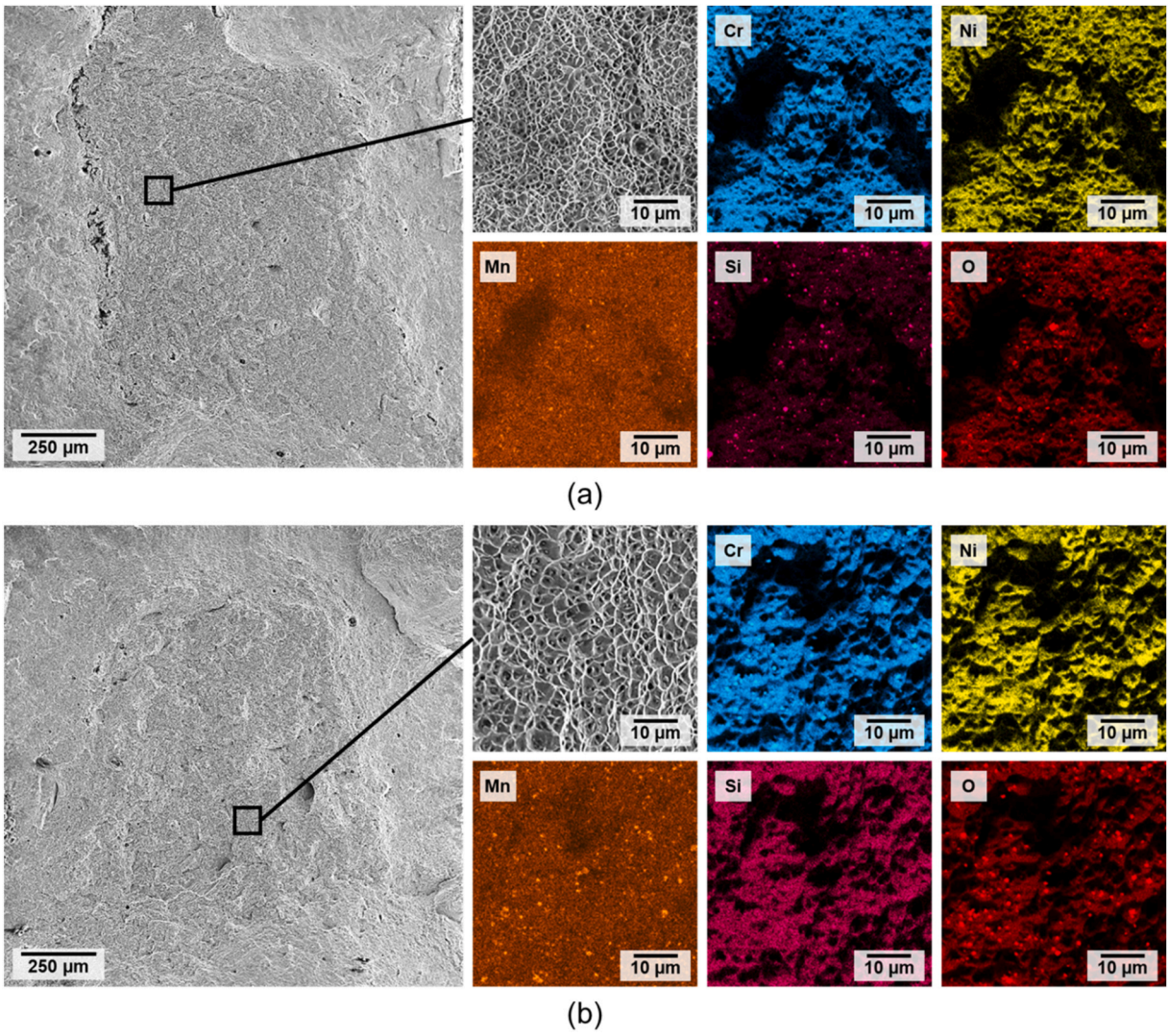

Fig. 7. SEM images and EDS elemental maps of tensile fracture surfaces showing a representative super grade duplex stainless steel alloy in the longitudinal orientation for the (a) as-deposited, and (b) post-processed HIP conditions.

grades, as shown in Fig. 8 and listed in Table 2. For example, the standard and super DSS grades displayed impact energies of only 13 J ± 5 J and 16 J ± 9 J, respectively. Both DSS grades, therefore, fall below the minimum requirements [39] as well as measurements made on DSS wrought plate, which were 152 J ± 32 J for the standard grade and 144 J ± 36 J for the super grade.

Such low impact energies in the as-deposited materials are problematic but can be correlated to the presence of defects and non-uniform microstructures. The addition of a post-process HIP treatment has been shown to mitigate similar issues encountered in the room temperature mechanical testing of as-deposited materials and improve the low-temperature impact energy of the AM processed materials. For example, the average impact energy for the standard DSS grade increased to 50 J ± 27 J from a level of 13 J ± 5 J in the as-deposited condition. Although the mean impact energy value for the standard grade just exceeded the standard requirement of 45 J, only three of the six samples tested exceeded 45 J. In contrast, the super DSS grade displayed a smaller increase after HIP, reaching an average impact energy of only 27 J ± 11 J, and none of the six samples tested met the 45 J standard requirement.

These decreased impact energies in the AM fabricated materials can be traced to the features that appear on the fracture surfaces obtained from the as-deposited and post-processed HIP DSS materials. In Fig. 9(a) and (b), the fracture surfaces are shown for the AM super DSS grade in the as-deposited and post-process HIP conditions, respectively. While the fracture surfaces of tensile specimens tested at room temperature displayed ductile dimpling exclusively, the fracture surfaces obtained from impact testing at low temperatures displayed both ductile dimpling as well as brittle cleavage features.

The appearance of these different fracture modes can be correlated to local changes in the ferrite and austenite phase distribution that can be captured by compositional variations on each fracture surface. As shown in Fig. 9(a) and (b), regions enriched in Cr were associated with the brittle cleavage areas on the fracture surfaces, consistent with the presence of ferrite. In contrast, the ductile, dimpled regions were enriched in Ni, indicating austenite. This compositional partitioning aligns with the known deformation behavior of these phases, where ferrite, with its body-centered cubic structure, tends to fracture in a brittle manner at low temperatures, while austenite, with its face-centered cubic structure, typically exhibits ductile failure [1].

Compositional maps obtained from these same fracture surfaces in the as-deposited and HIP post-processed materials also revealed a network of oxygen-rich inclusions not observed in the wrought material. These oxygen-rich inclusions form because of the high levels of oxygen

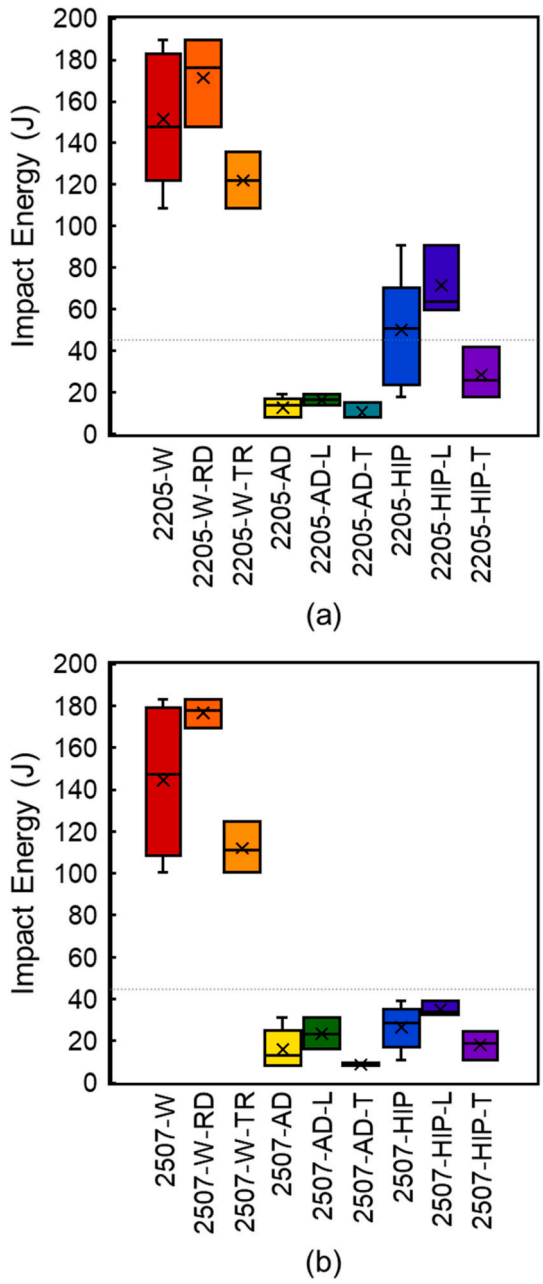

Fig. 8. Summary of Charpy impact data tested at −46 °C for the (a) standard and (b) super grades of duplex stainless steel materials. The standard requirement [39] is represented by the dotted line. X-axis labels follow the format alloy-condition-orientation (e.g., 2205-AD-L): alloy (2205 or 2507), condition (W: wrought, AD: as-deposited, HIP: hot isostatically pressed), and orientation (RD: rolling direction, TR: transverse rolling direction, L: longitudinal, T: transverse). When orientation is not specified, the dataset includes specimens from both orientations.

present in both the powder feedstock and the corresponding AM materials. In fact, the standard and super DSS grades displayed between 5 and 20 times, respectively, higher oxygen mass fractions than the corresponding wrought materials, as listed in Table 1. Measurements of the size of individual inclusions, which are summarized in Table 3, are similar in both the as-deposited and HIP post-processed conditions for each grade, with the inclusion size for the super DSS grade being slightly higher.

A more complete representation of inclusion size distributions is provided in Fig. 10(a) and (b) for the standard and super grades, respectively. A majority of the inclusions in both DSS grades are less than 600 nm in size, but subtle differences are observed when comparing the size distributions measured in the as-deposited and post-process HIP materials for each grade. As-deposited materials displayed a higher frequency of inclusions in the 300 nm to 500 nm size range for each grade, with the super DSS grade exhibiting the most prominent increase. Although these changes indicate that HIP affects the inclusion population, the magnitude of the changes is modest and is unlikely to be the primary cause of the observed improvement in impact energy after post-processing.

In addition to the measurement of the oxide inclusions, the grain structure and morphologies of the ferrite and austenite phases, particularly those near the fracture surface, are also impacted by the change in DSS grade and processing conditions. The locations of the deposition layers, grain structures, and ferrite and austenite phases are captured when viewing the profiles of the fracture surfaces, which are shown in Fig. 11. By visualizing the profile view of the fracture surface, the direction of crack propagation from the notch was tracked and correlated with the features in the surrounding microstructure. Clear differences in ferrite and austenite morphologies are visible for the different processing conditions and orientations. In the as-deposited condition, for example, the outlines of the deposition layers are evident in the longitudinal and transverse orientations shown in Fig. 11(a) and (b), respectively. Along both orientations, the ferrite grains appeared elongated in a direction parallel to the build height direction, which corresponds to the direction of heat flow, and were surrounded by grain boundary austenite with fine intragranular austenite within the ferrite grains.

These changes in grain morphology and orientation impacted the crack propagation path in the as-deposited samples. Within the longitudinally oriented samples, the elongated ferrite grains were parallel to the loading direction, allowing the crack path to proceed relatively unobstructed through the brittle ferrite and fine intragranular austenite, as shown in Fig. 11(a). Significant differences in crack path, however, were evident in the transverse orientation shown in Fig. 11(b). The crack path appeared to change direction when it encountered the larger austenite phases residing on the ferrite grain boundaries. However, there is a clear region along the crack path that displayed a much less tortuous path, in which the crack ran along individual deposition layers that contained lack-of-fusion defects highlighted by the presence of partially melted powder particles within the fracture surface, shown in Fig. 11(b). These qualitative observations were quantified by measuring the two-dimensional fracture length from profile view images of unetched samples. The as-deposited longitudinal samples exhibited an average fracture length of 9.28 ± 0.13 mm, whereas the as-deposited transverse samples exhibited an average fracture length of 9.07 ± 0.01 mm. These measurements indicate that the transverse fracture path was slightly shorter and less tortuous in the profile view and is consistent with preferential crack propagation along deposition layers containing process-related lack-of-fusion defects, even though austenite located along ferrite grain boundaries may contribute to local crack deflection.

The addition of a post-process HIP step produced a more uniform microstructure and, in turn, a more tortuous crack propagation path, as shown in Fig. 11(c) and (d) along the longitudinal and transverse orientations, respectively. These qualitative observations were quantified by measuring the two-dimensional fracture length from profile view images of unetched samples. The as-deposited samples exhibited an average fracture length of 9.22 ± 0.22 mm, whereas the HIP-treated samples exhibited a greater average fracture length of 9.94 ± 0.05 mm, consistent with a more tortuous crack path. Spatial variations in the ferrite and austenite regions were also eliminated, with

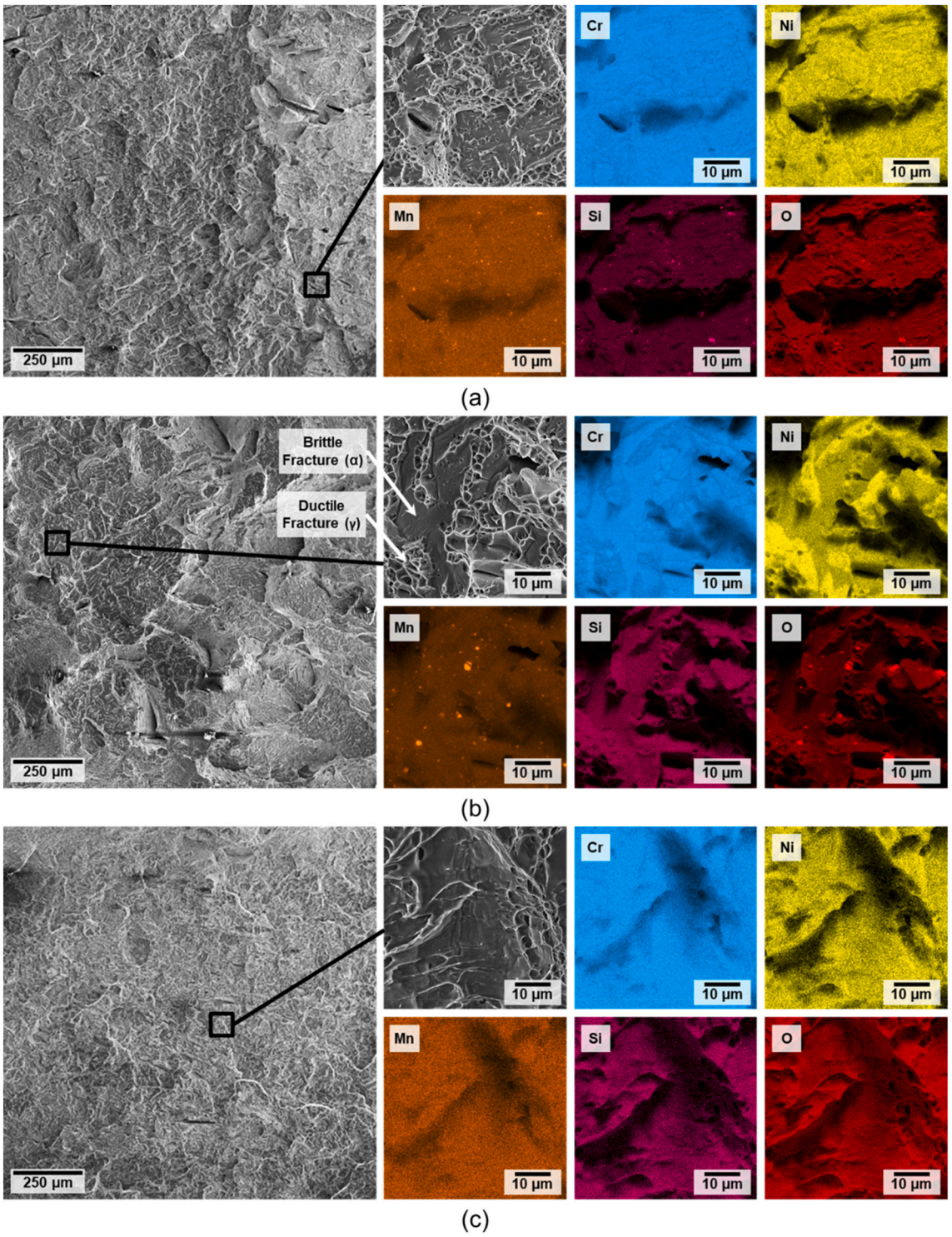

Fig. 9. SEM images and EDS elemental maps of Charpy impact fracture surfaces showing a representative super grade duplex stainless steel alloy in the longitudinal orientation for the (a) as-deposited, (b) post-processed HIP, (c) and wrought conditions.

the austenite morphology becoming more similar in appearance to wrought alloys but without the elongation produced during rolling [1].

Both the nominal austenite fractions and grain sizes increased from the as-deposited condition, as listed in Table 3. The crack path appeared to cut through and run parallel to elongated austenite features, suggesting enhanced crack deflection and increased resistance to propagation. The more uniform microstructure, increased austenite fractions, and elimination of process-related defects, contributed to the formation of a more tortuous crack path and improved low-temperature Charpy impact energy compared to the as-deposited condition.

While the addition of a HIP post-processing step led to microstructural improvements, the oxide inclusions observed in the as-deposited condition remained. Computational thermodynamic simulations combined with high-resolution TEM investigations have previously shown that these oxide inclusions form at high temperatures, often within the liquid phase, and remain stable across all practical heat treatment

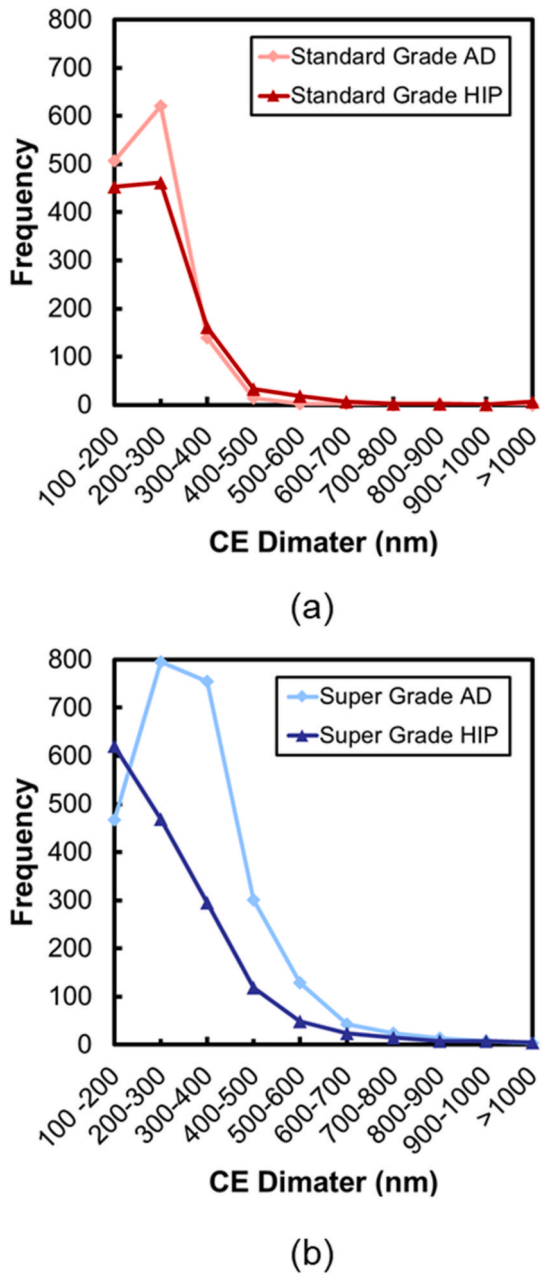

Fig. 10. Oxygen-rich inclusion size distributions in the as-deposited and post-processed HIP conditions for the (a) standard and (b) super grades. An area of 46,638 μm^2 was analyzed for each material condition.

temperatures, preventing their removal through post-process heat treatments [25]. Similar oxide-based inclusions have been associated with reduced Charpy impact energy in several other stainless steel systems, although the severity of the effect depends strongly on alloy chemistry, processing pathways, and post-processing treatments [42, 55–57].

Given the high number density of oxygen-rich inclusions observed within the DSS microstructures, they likely contributed to the degradation in low-temperature Charpy impact energy. Although the primary ferrite and austenite microstructures in both DSS grades displayed similar morphologies, phase fractions, and grain sizes, significant variations in oxygen content led to differences in the number and size of oxide inclusions. The standard grade, with a lower oxygen content, showed fewer and smaller inclusions and a higher nominal impact energy. In contrast, the super grade, with a higher oxygen content, contained larger and more numerous inclusions, leading to reduced impact energy.

4. Summary and conclusions

While the nominal room-temperature tensile properties of the DSS alloys fabricated using DED-L AM generally met the minimum standard requirements, low-temperature Charpy impact testing revealed qualification-relevant limitations that were not captured by room-temperature tensile testing alone. In the as-deposited condition, a combination of oxygen-rich inclusions, non-uniform microstructures, and lack-of-fusion defects significantly degraded the low-temperature impact properties. Post-process HIP mitigated several of these factors, such as minimizing defects and homogenizing the microstructure, leading to an increase in the impact energies compared to the as-deposited condition. However, thermodynamically stable oxide inclusions, driven by elevated oxygen levels in the powder feedstock, persisted after HIP, and contributed to impact energies of post-processed HIP materials well below corresponding wrought values. Powder feedstock chemistry, particularly oxygen content, should be considered when evaluating AM DSS components for harsh-environment applications. The primary conclusions are as follows:

- The nominal room temperature yield strength, ultimate tensile strength, and elongation at failure for the as-deposited conditions for both DSS grades met the minimum standard requirements. However, the values for the elongation to failure in the transverse orientation for the standard DSS grade were more than 65 % lower than in the longitudinal orientation because lack-of-fusion defects were aligned along the deposition layers.
- The addition of a post-process HIP produced room temperature tensile properties that were similar to traditional wrought alloys and met the minimum standard requirements. No process-related defects were detected after HIP, which contributed to the improved elongation at failure values compared to the as-deposited values.
- Low-temperature impact properties were approximately one-third of the standard minimum values in the as-deposited condition. These low values were linked to the microstructure, which was characterized by high fractions of oxide inclusions, fine austenite grain sizes, and process-related defects, leading to a significant degradation in the impact properties.
- Post-process HIP reduced process-related defects, increased both austenite phase fraction and grain size, which improved the impact properties compared to the as-deposited condition. While improvements in impact energies were observed, they were well below wrought values, indicating that defect reduction and phase-balance improvements alone were insufficient to restore impact energies to wrought levels.
- The high number density of oxygen-rich inclusions persisted after HIP and was attributed to the reduced low-temperature impact performance.

CRediT authorship contribution statement

A.D. Iams: Conceptualization, Data curation, Formal analysis, Investigation, Methodology, Writing – original draft. **T.A. Palmer:** Conceptualization, Funding acquisition, Methodology, Writing – review & editing.

Declaration of competing interest

The authors declare that they have no known competing financial interests or personal relationships that could have appeared to influence the work reported in this paper.

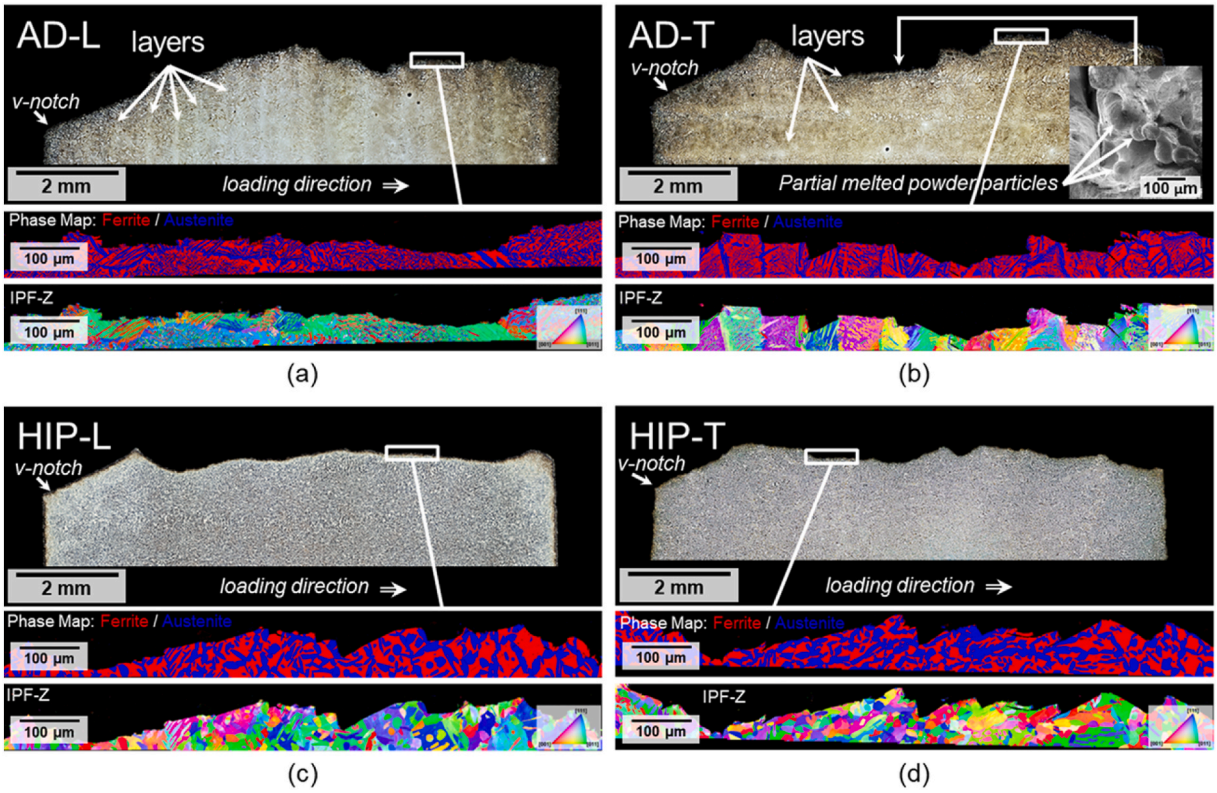

Fig. 11. A representative profile view of broken Charpy impact samples in the (a)(c) longitudinal and (b)(d) transverse orientations of a standard grade of duplex stainless steel in the (a)(b) as-deposited and (c)(d) post-process HIP conditions.

Acknowledgements

A. D. Iams acknowledges the support from the American Welding Society Foundation Research Fellowship. The authors acknowledge the Office of Naval Research Manufacturing Technology program and the Applied Research Laboratory's Institute for Manufacturing and Sustainment Technologies that is funded under the Naval Sea Systems Command (NAVSEA) contract #N00024-12-D-6404. The authors thank the Center for Innovative Materials Processing through Direct Digital Deposition (CIMP-3D) for the use of their equipment and Mr. Jay Tressler for fabricating the builds. Mr. Tim Stecko, Ms. Whitney Yetter, and Dr. Mingze Gao are also acknowledged for their support with X-ray CT scans, and the porosity analysis. We also acknowledge Mr. Magnus Ahlfors at Quintus Technologies for performing the hot isostatic pressing of the AM materials. Finally, the authors thank Dr. James S. Zuback and Dr. Ian J. Wietecha-Reiman for the helpful discussions and review of this manuscript.

Appendix A

Table A1
A summary of tensile property data for additively manufactured (AM) duplex stainless steels.

Material	AM Process	Condition	Ferrite Fraction (%)	Orientation[a]	Yield Strength (MPa)	UTS (MPa)	Elongation at Fracture[b] (%)	Ref.
2205	PBF-L	AD	99	T	940[c]	940	12	[8]
		HT: 900 °C/5 min.	76	T	600[c]	767[c]	22[c]	[8]
		HT: 1000 °C/5 min.	66	T	600[c]	776[c]	27[c]	[8]
		HT: 1200 °C/5 min.	79	T	580[c]	719[c]	24[c]	[8]
2205	PBF-L	AD	99	T	950.0 ± 9.2	1071.3 ± 6.9	16.0 ± 1.1	[9]
		HT: 950 °C/5 min	59.9	T	560.8 ± 3.3	868.7 ± 2.3	39.7 ± 1.6	[9]
		HT: 1000 °C/5 min	56.8	T	549.0 ± 4.9	848.0 ± 1.0	45.8 ± 2.6	[9]
		HT: 1050 °C/5 min	57.0	T	535.5 ± 9.2	836.7 ± 1.1	42.1 ± 3.5	[9]
		HT: 1100 °C/5 min	57.4	T	524.0 ± 2.8	813.0 ± 0.6	39.7 ± 3.4	[9]
		HT: 1000 °C/1 h	53.6	T	531.7 ± 2.5	824.4 ± 1.8	43.4 ± 2.5	[9]
		HT: 1050 °C/1 h	54.6	T	517.1 ± 2.9	812.1 ± 4.1	41.8 ± 1.5	[9]
2205	PBF-L	AD	ferritic	T	773 ± 14	865 ± 19	8 ± 1	[14]
		HT: 1050 °C/3 h	64	T	558 ± 7	750 ± 9	28 ± 6	[14]
		HIP: 1150 °C/110 MPa/3 h + HT: 1050 °C/3 h	60	T	548 ± 5	730 ± 19	26 ± 5	[14]

(*continued on next page*)

Table A1 (*continued*)

Material	AM Process	Condition	Ferrite Fraction (%)	Orientation[a]	Yield Strength (MPa)	UTS (MPa)	Elongation at Fracture[b] (%)	Ref.
2205	PBF-L	AD	99.3	---	826 ± 32	872 ± 33	11 ± 2	[10]
		HT: 1100 °C/1 h	51-56	---	465 ± 3	622 ± 19	21.3 ± 1.4	[10]
2507	PBF-L	AD	98	---	1214 ± 43	1321 ± 48	>45	[11]
2507	PBF-L	AD	ferritic	T	913 ± 16	1031 ± 18	14 ± 2	[14]
		HT: 1050 °C/3 h	57	T	670 ± 14	859 ± 8	35 ± 3	[14]
		HIP: 1150 °C/110 MPa/3 h + HT: 1050 °C/3 h	57	T	607 ± 25	802 ± 12	43 ± 3	[14]
2205	PBF-L	AD	98.5	---	1391 ± 9	1493 ± 6	13.2 ± 1	[12]
		HT: 1100 °C/1 h	59.5	---	665 ± 7	941 ± 10	24.6 ± 2	[12]
		HT: 1150 °C/1 h	61.4	---	658 ± 10	901 ± 4	36.4 ± 2	[12]
		HT: 1200 °C/1 h	63.4	---	646 ± 3	893 ± 1	38.7 ± 2	[12]
2205	PBF-L	AD	99.8	---	1163	1368	5	[15]
		HT: 1000 °C/1 h	39.7	---	622	880	29	[15]
		HT: 1100 °C/1 h	42.4	---	579	847	28	[15]
		HT: 1200 °C/1 h	43.4	---	564	820	30	[15]
2205	PBF-L	AD	100	L	523 ± 6	832 ± 6	36.9 ± 2.2	[13]
				T	482 ± 7	753 ± 8	52.1 ± 2.7	[13]
2205	PBF-L	AD	98	---	651 ± 6	844 ± 5	18 ± 1	[16]
		HT: 1000 °C/10 min	55	---	563 ± 15	798 ± 5	28 ± 2	[16]
2209	WAAM	AD	25 to 30	L	505 to 510	818 to 743	–	[29]
				T	480	682	–	[29]
2209	WAAM	AD	26 to 29	T	455	717	28	[30]
2209	WAAM	AD	37 to 40	T	521 to 549	726 to 733	33 to 35	[31]
2209	WAAM	AD	36.9 to 55.1	L	450 to 650[c]	695 to 861	~32.8 to 43.5	[38]
2594	WAAM	AD	15 to 27	T	510 to 555[c]	790 to 815[c]	31 to 36[c]	[32]
				L	550 to 600[c]	830 to 860[c]	27 to 31[c]	[32]
2594	WAAM	AD	1.6	T	500 to 560[c]	820 to 850[c]	35 to 38[c]	[33]
				L	550 to 600[c]	905 to 920[c]	33 to 35[c]	[33]
2594	WAAM	AD	28 to 44	L	735.6 ± 9.20	1075.92 ± 9.61	38.45 ± 0.97	[34]
				T	684.86 ± 11.72	1001.05 ± 8.74	35.10 ± 1.61	[34]
2594	WAAM	AD	25 to 33	L	632 ± 13	855 ± 11	44.3 ± 2.5	[35]
				45° between L and T	607 ± 11	837 ± 15	42.9 ± 1.7	[35]
				T	622 ± 12	838 ± 15	48.2 ± 2.2	[35]
2209	WAAM	AD	18 to 49[c]	L	530	769	31[c]	[36]
		Gas: Ar		T	488	714	40[c]	[36]
		AD	14 to 38[c]	L	538	814	21[c]	[36]
		Gas: Ar + 2 % O_2		T	459	667	35[c]	[36]
		AD	24 to 42[c]	L	539	826	26[c]	[36]
		Gas: Ar + 2 % N_2		T	490	751	31[c]	[36]
2594	WAAM	AD	37.2	L	933	1013	27.7	[37]
				T	860	941	25.2	[37]
2209	WAAM	AD	26 to 30	L	468 ± 5	743 ± 6	19 ± 1	[27]
				T	451 ± 3	701 ± 5	29 ± 1	[27]
			22 to 26	L	447 ± 12	727 ± 12	21 ± 2	[27]
				T	440 ± 4	709 ± 9	28 ± 3	[27]
			23 to 28	L	459 ± 8	716 ± 18	18	[27]
				T	452 ± 16	707 ± 7	28 ± 2	[27]
2209	DED-L	AD	48 to 67	L	697 to 722	846 to 846	25.2 to 28.0	[21]
		HT: 1100 °C/1 h	49.4	L	481 to 493	751 to 756	32.6 to 35.2	[21]
2507	DED-L	AD	55	L	820 ± 35	950 ± 21	15 ± 3	[26]
2209	DED-L	AD	48	L	706	851	26	[22]
		HT: 1100 °C/1 h	51	L	487	753	34	[22]
		AD	67	L	726	833	21	[22]
				T	749	858	22	[22]
		HT: 1100 °C/1 h	50	L	528	758	34	[22]
				T	499	745	32	[22]
2205	DED-L	AD	50.1	T	740[c]	904[c]	29[c]	[23]
			60.4	T	815[c]	936[c]	25[c]	[23]
			42.6	T	730[c]	824[c]	32[c]	[23]

Notes:
(a) Orientation is defined according to schematic shown in Fig. 3, where, L = longitudinal, T = transverse.
(b) Some data were obtained using miniature tensile specimens, which can provide comparable yield and ultimate tensile strength values to standard specimens [28]. However, elongation is sensitive to specimen geometry [28] and should therefore be interpreted with caution.
(c) Value estimated from published figures using graphical data extraction; original numerical values were not reported.

Table A2
A summary of available full-size Charpy impact data from additively manufactured duplex stainless steel.

Material	AM Process	Condition	Mass Fraction Oxygen (%)	Ferrite Fraction (%)	Orientation[a]	Test Temp. (°C)	Impact Energy[b] (J)	Ref.
2209	WAAM	AD	0.041	26 to 29	L	Room temp.	70	[30]
2594	WAAM	AD	---	~17 to 23	L	−20	93 to 108[c]	[32]
2205	PBF-L	AD	0.018	98.5	---	Room temp.	18 ± 3	[12]
		HT: 1150 °C/1 h	0.018	61.4	---	Room temp.	132 ± 5	[12]
2209	WAAM	AD	---	24.7	L	−40	59.1	[40]
2209	WAAM	AD	---	26.4	L	−40	56.4	[40]
2209	DED-L	AD	0.006[d]	48-67	L	−10	230[d]	[21]
					T	−10	206[d]	[21]
		HT: 1100 °C/1 h	0.007[d]	49.4	L	−10	260[d]	[21]
					T	−10	239[d]	[21]
2209	DED-L	AD	---	48	L	−10	230	[22]
					T	−10	205	[22]
		HT: 1100 °C/1 h	---	51	L	−10	260	[22]
					T	−10	239	[22]
	DED-L	AD	---	67	L	−10	268	[22]
					T	−10	163	[22]
		HT: 1100 °C/1 h	---	50	L	−10	295	[22]
					T	−10	191	[22]
2594	WAAM	AD	---	37.2	L	25	229	[37]
					T	25	228	[37]
2205	PBF-L	AM Atmosphere: Ar 99 %/HIP:1145 °C/103 MPa/ 185 min + HT: 1080 °C/60 min	0.049	58	T	−196	6.7 ± 0.1	[17]
						−40	80.5 ± 3.4	[17]
						20	137.2 ± 25	[17]
						150	169.5 ± 9.2	[17]
		AM Atmosphere: N_2 99 %/HIP:1145 °C/103 MPa/ 185 min + HT: 1080 °C/60 min	0.050	57	T	−196	6.8 ± 0.2	[17]
						−40	81.5 ± 11.6	[17]
						20	138.3 ± 5.5	[17]
						150	151.9 ± 10	[17]

Note:
(a) Orientation is defined according to schematic shown in Fig. 3, where, L = longitudinal, T = transverse.
(b) Data reported for full size Charpy samples (10 mm × 10 mm x 55 mm).
(c) Value estimated from published figures using graphical data extraction; original numerical values were not reported.
(d) This value represents an average from published values.

Data availability

Data will be made available on request.

References

[1] I. Alvarez-Armas, S. Degallaix-Moreuil, Duplex Stainless Steels, ISTE ; J. Wiley, 2009, 1118599918, 9781118599914.
[2] L. Karlsson, Welding Duplex Stainless Steels — a Review of Current Recommendations, 5, 2012, pp. 65–76, https://doi.org/10.1007/BF03321351.
[3] J.W. Elmer, T.A. Palmer, E.D. Specht, Direct Observations of Sigma Phase Formation in Duplex Stainless Steels Using in Situ Synchrotron X-Ray Diffraction, 2006, pp. 464–475, https://doi.org/10.1007/s11661-006-9076-3.
[4] V. Muthupandi, P. Bala Srinivasan, S.K. Seshadri, S. Sundaresan, Corrosion behaviour of duplex stainless steel weld metals with nitrogen additions, in: Corrosion Engineering Science and Technology, 2003, pp. 303–308, https://doi.org/10.1179/147842203225008895.
[5] V. Muthupandi, P. Bala Srinivasan, S.K. Seshadri, S. Sundaresan, Effect of weld metal chemistry and heat input on the structure and properties of duplex stainless steel welds, Mater. Sci. Eng., A 358 (2003) 9–16, https://doi.org/10.1016/S0921-5093(03)00077-7.
[6] T. DebRoy, H.L. Wei, J.S. Zuback, T. Mukherjee, J.W. Elmer, J.O. Milewski, A. M. Beese, A. Wilson-Heid, A. De, W. Zhang, Additive manufacturing of metallic components – process, structure and properties, Prog. Mater. Sci. 92 (2018) 112–224, https://doi.org/10.1016/j.pmatsci.2017.10.001.
[7] K.P. Davidson, S.B. Singamneni, Metallographic evaluation of duplex stainless steel powders processed by selective laser melting, Rapid Prototyp. J. 23 (2017) 1146–1163, https://doi.org/10.1108/RPJ-04-2016-0053.
[8] F. Hengsbach, P. Koppa, K. Duschik, M.J. Holzweissig, M. Burns, J. Nellesen, W. Tillmann, T. Tröster, K.P. Hoyer, M. Schaper, Duplex stainless steel fabricated by selective laser melting - microstructural and mechanical properties, Mater. Des. 133 (2017) 136–142, https://doi.org/10.1016/j.matdes.2017.07.046.
[9] S. Papula, M. Song, A. Pateras, X.B. Chen, M. Brandt, M. Easton, Y. Yagodzinskyy, I. Virkkunen, H. Hänninen, Selective laser melting of duplex stainless steel 2205: effect of post-processing heat treatment on microstructure, mechanical properties, and corrosion resistance, Materials 12 (2019), https://doi.org/10.3390/ma12152468.
[10] G.N. Nigon, O. Burkan Isgor, S. Pasebani, The effect of annealing on the selective laser melting of 2205 duplex stainless steel: microstructure, grain orientation, and manufacturing challenges, Opt. Laser Technol. 134 (2021), https://doi.org/10.1016/j.optlastec.2020.106643.
[11] K. Saeidi, L. Kevetkova, F. Lofaj, Z. Shen, Novel ferritic stainless steel formed by laser melting from duplex stainless steel powder with advanced mechanical properties and high ductility, Mater. Sci. Eng., A 665 (2016) 59–65, https://doi.org/10.1016/j.msea.2016.04.027.
[12] F. Shang, X. Chen, Z. Wang, Z. Ji, F. Ming, S. Ren, X. Qu, The microstructure, mechanical properties, and corrosion resistance of UNS S32707 hyper-duplex stainless steel processed by selective laser melting, Metals (Basel). 9 (2019), https://doi.org/10.3390/met9091012.
[13] S. Jeffs, R. Douglas, W. Beard, M. Coleman, J. Adams, T. Jones, D. Poole, R. Lancaster, Characterising the high temperature tensile behaviour of laser powder bed fused duplex stainless steel 2205 using the small punch test, Mater. Charact. 189 (2022), https://doi.org/10.1016/j.matchar.2022.111953.
[14] J. Kunz, A. Boontanom, S. Herzog, P. Suwanpinij, A. Kaletsch, C. Broeckmann, Influence of hot isostatic pressing post-treatment on the microstructure and mechanical behavior of standard and super duplex stainless steel produced by laser powder bed fusion, Mater. Sci. Eng., A 794 (2020), https://doi.org/10.1016/j.msea.2020.139806.
[15] H. Xiang, W. Zhao, Y. Lu, Effect of solution temperature on microstructure and mechanical properties of selective laser melted Fe-22Cr-5Ni-0.26N duplex stainless steel, J. Mater. Res. Technol. 19 (2022) 1379–1389, https://doi.org/10.1016/j.jmrt.2022.05.124.
[16] N. Haghdadi, C. Ledermueller, H. Chen, Z. Chen, Q. Liu, X. Li, G. Rohrer, X. Liao, S. Ringer, S. Primig, Evolution of microstructure and mechanical properties in 2205 duplex stainless steels during additive manufacturing and heat treatment, Mater. Sci. Eng., A 835 (2022), https://doi.org/10.1016/j.msea.2022.142695.
[17] J.S. Koob, C. Broeckmann, A. Kaletsch, Influence of process atmosphere and high initial porosity introduced by laser powder bed fusion on the impact toughness of hot isostatically post-densified 2205 duplex stainless steel, Mater. Sci. Eng., A 941 (2025), https://doi.org/10.1016/j.msea.2025.148633.

[18] W. Zhao, H. Xiang, X. Zhang, X. Zhan, F. Zhang, C. Wu, Y. Lu, Y. Lu, Deformation behavior and recrystallization mechanism of a duplex stainless steel fabricated by laser powder bed fusion at high-temperature uniaxial tensile test, Mater. Sci. Eng., A 946 (2025), https://doi.org/10.1016/j.msea.2025.149153.
[19] J. Kangazian, S.Y. Ahn, B.W. Koo, J.H. Lee, M.J. SaGong, R. Wu, D.W. Lee, L. Xu, H. H. Lee, D.W. Suh, H.S. Kim, Hydrogen embrittlement mitigation via microstructural and phase control in laser powder bed–fused SAF 3207 hyper duplex stainless steel, Mater. Sci. Eng., A 955 (2026), https://doi.org/10.1016/j.msea.2026.149861.
[20] J.H. Wen, L.J. Zhang, J. Ning, F. Xue, X.W. Lei, J.X. Zhang, S.J. Na, Laser additively manufactured intensive dual-phase steels and their microstructures, properties and corrosion resistance, Mater. Des. 192 (2020), https://doi.org/10.1016/j.matdes.2020.108710.
[21] A. Baghdadchi, V.A. Hosseini, M.A. Valiente Bermejo, B. Axelsson, E. Harati, M. Högström, L. Karlsson, Wire laser metal deposition of 22% Cr duplex stainless steel: as-deposited and heat-treated microstructure and mechanical properties, J. Mater. Sci. 57 (2022) 9556–9575, https://doi.org/10.1007/s10853-022-06878-6.
[22] A. Baghdadchi, V.A. Hosseini, M.A.V. Bermejo, B. Axelsson, E. Harati, M. Högström, L. Karlsson, Wire laser metal deposition additive manufacturing of duplex stainless steel components—development of a systematic methodology, Materials 14 (2021), https://doi.org/10.3390/ma14237170.
[23] G. Luo, Z. Zhao, J. Peng, X. Deng, Y. Li, X. Liu, M. Cheng, S. Li, L. Song, Developing a novel phase balance of duplex stainless steel for exceptional mechanical properties and corrosion resistance, Scr. Mater. 257 (2025), https://doi.org/10.1016/j.scriptamat.2024.116467.
[24] A.D. Iams, J.S. Keist, T.A. Palmer, Formation of austenite in additively manufactured and post-processed duplex stainless steel alloys, Metall. Mater. Trans. A Phys. Metall. Mater. Sci. 51 (2020) 982–999, https://doi.org/10.1007/s11661-019-05562-w.
[25] A.D. Iams, J.S. Keist, L.A. Giannuzzi, T.A. Palmer, The evolution of oxygen-based inclusions in an additively manufactured super-duplex stainless steel, Metall. Mater. Trans. A Phys. Metall. Mater. Sci. 52 (2021) 3401–3412, https://doi.org/10.1007/s11661-021-06311-8.
[26] D. Jiang, X. Gao, Y. Zhu, C. Hutchinson, A. Huang, In-situ duplex structure formation and high tensile strength of super duplex stainless steel produced by directed laser deposition, Mater. Sci. Eng., A 833 (2022), https://doi.org/10.1016/j.msea.2021.142557.
[27] V. Mahey, G.A. Johnson, P. Burad, R. Chulist, P.C. Collins, S. Roy, Large-scale wire arc additive manufacturing of duplex stainless steel: comprehensive insights into microstructure and mechanical behavior, Mater. Sci. Eng., A 963 (2026) 150232, https://doi.org/10.1016/j.msea.2026.150232.
[28] J. Dzugan, E. Lucon, M. Koukolikova, Y. Li, S. Rzepa, M.S. Yasin, S. Shao, N. Shamsaei, M. Seifi, M. Lodeiro, F. Lefebvre, U. Mayer, J. Olbricht, M. Houska, V. Mentl, Z. You, ASTM interlaboratory study on tensile testing of AM deposited and wrought steel using miniature specimens, Theor. Appl. Fract. Mech. 131 (2024), https://doi.org/10.1016/j.tafmec.2024.104410.
[29] F. Hejripour, F. Binesh, M. Hebel, D.K. Aidun, Thermal modeling and characterization of wire arc additive manufactured duplex stainless steel, J. Mater. Process. Technol. 272 (2019) 58–71, https://doi.org/10.1016/j.jmatprotec.2019.05.003.
[30] G. Posch, K. Chladil, H. Chladil, Material properties of CMT—Metal additive manufactured duplex stainless steel blade-like geometries, Weld. World 61 (2017) 873–882, https://doi.org/10.1007/s40194-017-0474-5.
[31] F. Binesh, A. Bahrami, M. Hebel, D.K. Aidun, Preservation of natural phase balance in multi-pass and wire arc additive manufacturing-made duplex stainless steel structures, J. Mater. Eng. Perform. 30 (2021) 2552–2565, https://doi.org/10.1007/s11665-021-05593-8.
[32] M. Lervåg, C. Sørensen, A. Robertstad, B.M. Brønstad, B. Nyhus, M. Eriksson, R. Aune, X. Ren, O.M. Akselsen, I. Bunaziv, Additive manufacturing with superduplex stainless steel wire by cmt process, Metals (Basel). 10 (2020), https://doi.org/10.3390/met10020272.
[33] X. Zhang, K. Wang, Q. Zhou, J. Ding, S. Ganguly, M. Grasso, D. Yang, X. Xu, P. Dirisu, S.W. Williams, Microstructure and mechanical properties of TOP-TIG-wire and arc additive manufactured super duplex stainless steel (ER2594), Mater. Sci. Eng., A 762 (2019), https://doi.org/10.1016/j.msea.2019.138097.
[34] A.R. Kannan, N.S. Shanmugam, K.D. Ramkumar, V. Rajkumar, Studies on super duplex stainless steel manufactured by wire Arc additive manufacturing, Trans. Indian Inst. Met. 74 (2021) 1673–1681, https://doi.org/10.1007/s12666-021-02257-y.
[35] P.P. Nikam, D. Arun, K.D. Ramkumar, N. Sivashanmugam, Microstructure characterization and tensile properties of CMT-based wire plus arc additive manufactured ER2594, Mater. Charact. 169 (2020), https://doi.org/10.1016/j.matchar.2020.110671.
[36] E. Akbarzadeh, K. Yurtışık, C. Hakan Gür, T. Saeid, R. Tavangar, Influence of shielding gas on the microstructure and mechanical properties of duplex stainless steel in wire arc additive manufacturing, Met. Mater. Int. 30 (2024) 1977–1996, https://doi.org/10.1007/s12540-023-01623-3.
[37] S. Wu, C. Guo, W. Liu, M. Ying, Y. Li, Wire arc additive manufacturing using ER2594 duplex stainless steel, Trans. Indian Inst. Met. 76 (2023) 249–258, https://doi.org/10.1007/s12666-022-02746-8.
[38] L. Yang, W. Lu, Z. Liu, Y. Zhang, F. Xu, H. Gao, Z. Yao, Location-dependent microstructure and properties for plasma Arc additively manufactured duplex stainless steel ER2209 wire, J. Mater. Eng. Perform. 30 (2021) 6788–6800, https://doi.org/10.1007/s11665-021-06005-7.
[39] The International Organization for Standardization, ISO 17781, Petroleum, Petrochemical and Natural Gas Industries - Test Methods for Quality Control of Microstructure of Ferritic/Austenitic (Duplex) Stainless, 2017.
[40] Y. Zhang, F. Cheng, S. Wu, The microstructure and mechanical properties of duplex stainless steel components fabricated via flux-cored wire arc-additive manufacturing, J. Manuf. Process. 69 (2021) 204–214, https://doi.org/10.1016/j.jmapro.2021.07.045.
[41] Y.H. Moon, H.T. Kim, S.D. Hur, Effect of oxygen content on impact toughness of austenitic-and duplex stainless steel weld metal, J. Korean Weld. Soc. 5 (1987) 38–45.
[42] E. Hämäläinen, A. Laitinen, H. Hänninen, J. Liimatainen, Mechanical properties of powder Metallurgy duplex stainless steels, Mater. Sci. Technol. 13 (1997) 103–109, https://doi.org/10.1179/mst.1997.13.2.103.
[43] ASTM International, ASTM A276/A276M, specification for stainless steel bars and shapes. https://doi.org/10.1520/A0276_A0276M-17, 2017.
[44] ASTM International, ASTM E1019, test methods for determination of carbon, sulfur, nitrogen, and oxygen in steel, iron, nickel, and cobalt alloys. Various Combustion and Fusion Techniques, ASTM International, West Conshohocken, PA, 2018, https://doi.org/10.1520/E1019-18.
[45] ASTM International, ASTM E1097, Guide for Determination of Various Elements by Direct Current Plasma Atomic Emission Spectrometry, ASTM International, West Conshohocken, PA, 2017, https://doi.org/10.1520/E1097-12R17.
[46] ASTM International, ASTM E8/E8M, Test Methods for Tension Testing of Metallic Materials, 2022, https://doi.org/10.1520/E0008_E0008M-22.
[47] ASTM International, ASTM E23, Test Methods for Notched bar Impact Testing of Metallic Materials, 2024, https://doi.org/10.1520/E0023-24.
[48] A.E. Wilson-Heid, A.M. Beese, Combined effects of porosity and stress state on the failure behavior of laser powder bed fusion stainless steel 316L, Addit. Manuf. 39 (2021), https://doi.org/10.1016/j.addma.2021.101862.
[49] M.C. Brennan, J.S. Keist, T.A. Palmer, Defects in metal additive manufacturing processes, J. Mater. Eng. Perform. 30 (2021) 4808–4818, https://doi.org/10.1007/s11665-021-05919-6.
[50] D.J. Shaffer, A.E. Wilson-Heid, J.S. Keist, A.M. Beese, T.A. Palmer, Impact of retained austenite on the aging response of additively manufactured 17-4 PH grade stainless steel, Mater. Sci. Eng., A 817 (2021), https://doi.org/10.1016/j.msea.2021.141363.
[51] S.D. Meredith, J.S. Zuback, J.S. Keist, T.A. Palmer, Impact of composition on the heat treatment response of additively manufactured 17–4 PH grade stainless steel, Mater. Sci. Eng., A 738 (2018) 44–56, https://doi.org/10.1016/j.msea.2018.09.066.
[52] Z.R. Khayat, T.A. Palmer, Impact of iron composition on the properties of an additively manufactured solid solution strengthened nickel base alloy, Mater. Sci. Eng., A 718 (2018) 123–134, https://doi.org/10.1016/j.msea.2018.01.112.
[53] J.S. Zuback, A.D. Iams, F. Zhang, L.A. Giannuzzi, T.A. Palmer, Stable nitride precipitation in additively manufactured nickel superalloys, J. Alloys Compd. 910 (2022), https://doi.org/10.1016/j.jallcom.2022.164918.
[54] I.J. Wietecha-Reiman, A.D. Iams, S.M. Sabol, T.A. Palmer, Contributions of sub-surface intergranular phases on fatigue crack initiation in additively manufactured austenitic stainless steel, J. Mater. Sci. 60 (2025) 18332–18351, https://doi.org/10.1007/s10853-025-11259-w.
[55] A.J. Cooper, N.I. Cooper, J. Dhers, A.H. Sherry, Effect of oxygen content upon the microstructural and mechanical properties of type 316L austenitic stainless steel manufactured by hot isostatic pressing, Metall. Mater. Trans. A Phys. Metall. Mater. Sci. 47 (2016) 4467–4475, https://doi.org/10.1007/s11661-016-3612-6.
[56] A. Plumtree, R. Gullberg, The Influence of Interstitial Content on the Ductile-Brittle Transition Temperature of Fe-25Cr Ferritic Stainless Steels, 1974.
[57] X. Lou, P.L. Andresen, R.B. Rebak, Oxide inclusions in laser additive manufactured stainless steel and their effects on impact toughness and stress corrosion cracking behavior, J. Nucl. Mater. 499 (2018) 182–190, https://doi.org/10.1016/j.jnucmat.2017.11.036.